Supplementary Material to Evidence of Extreme Ultraviolet Superfluorescence in Xenon

L. Mercadier,[1,2] A. Benediktovitch,[3] C. Weninger,[1] M. A. Blessenohl,[4] S. Bernitt,[5,4] H. Bekker,[4] S. Dobrodey,[4] A. Sanchez-Gonzalez,[6] B. Erk,[3] C. Bomme,[3] R. Boll,[3] Z. Yin,[3,7] V. P. Majety,[1] R. Steinbrügge,[4] M. A. Khalal,[8] F. Penent,[8] J. Palaudoux,[8] P. Lablanquie,[8] A. Rudenko,[9] D. Rolles,[3,9] J. R. Crespo López-Urrutia,[4] and N. Rohringer[1,3,10]

[1] *Max Planck Institute for the Structure and Dynamics of Matter, 22761 Hamburg, Germany*
[2] *European XFEL, 22869 Schenefeld, Germany*
[3] *Deutsches Elektronen-Synchrotron (DESY), 22761 Hamburg, Germany*
[4] *Max-Planck-Institut für Kernphysik, 69117 Heidelberg, Germany*
[5] *Institut für Optik und Quantenelektronik, Friedrich-Schiller-Universität Jena, 07743 Jena, Germany*
[6] *Department of Physics, Imperial College London, London SW7 2AZ, United Kingdom*
[7] *Max Planck für biophysikalische Chemie, 37077 Gttingen, Germany*
[8] *Laboratoire de Chimie Physique - Matière et Rayonnement, Université Pierre et Marie Curie, F-75231 Paris Cedex 05, France*
[9] *J. R. Macdonald Laboratory, Department of Physics, Kansas State University, Manhattan, KS 66506, USA*
[10] *Department of Physics, Universität Hamburg, 20355 Hamburg, Germany*

EXPERIMENTAL SETUP

The experiment was performed at the CAMP end station at FLASH. Pulses of $\sim 80-100$ fs duration at 10-Hz repetition rate were focused to a nominal spot of 5×7 μm^2 into a pressurized gas cell of 4.5 mm length along the beam axis, so that the excited gas has a pencil-shaped geometry of large aspect ratio. The experiment was performed on both Xe and Kr gases (only Xe results are presented in the main text). The photon energy was tuned to 73 eV, 92 eV and 100 eV for Xe studies, and 100 eV for Kr. Assuming a beamline transmission of 50%, the maximum available pulse energy on target was 90 μJ, corresponding to an intensity of 4×10^{15} W cm^{-2}. The gas cell of adjustable pressure was used in previous experiments and consisted of three sections delimited by four Kapton windows. The central section of 4.5-mm length contained gas at 1-100 mbar pressure, while the two outer sections were used for differential vacuum pumping, ensuring a residual pressure in the main chamber below 10^{-5} mbar. The transmitted pulse and stimulated emission were impinging on a high resolution spectrometer consisting of a rotatable parabolic Pt-coated grating with 2400 grooves/mm and a radius of curvature of 3 m. The diffracted light was imaged onto a CCD camera (Andor, model Newton) at a fixed angle of 15° with the incoming arm. The selection of the diffraction order and wavelength range of observation was achieved by rotating the grating. Given the large focal length of the spectrometer, the maximum solid angle detectable was 1.4×10^{-4} sr. The size of the excited medium was estimated from the focusing geometry of the spectrometer to 20 - 30 μm radius.

The spectrometer calibration consists of determining parameters A and B of the following equation, for small grating angles: $k\lambda = A\theta - Bx$ where λ is the wavelength, k is the diffraction order, θ is the grating angle with respect to 0^{th} order and x is the lateral position on the CCD in pixels. To do so, we performed absorption spectroscopy measurements of He auto-ionizing resonances (see Zubek et al., J. Phys. B: At., Mol. Opt. Phys. **22**, 3411 (1989) and Domke et al., Phys. Rev. A **53**, 1424 (1996)). With 80 mbar of He in the gas cell and a photon energy of 73 eV, we recorded spectra of self-amplified spontaneous emission (SASE) at different diffraction orders. For each order, averaging over a few hundred shots results in a smooth spectrum showing absorption dips at characteristic energies that we used for calibration. We found an angle dispersion of $A = (14.58 \pm 0.07)$ nm/deg, and a dispersion on the detector of $B = (1.70 \pm 0.02)$ pm/pixel, which corresponds to a resolution power of $\sim 2\times10^4$ and an observable wavelength window of ≈ 3.5 nm in 1^{st} order of diffraction. In 3^{rd} order, this translates to a resolution power of $\sim 6\times10^4$. The grating angle was manually adjustable and allowed the selection of the central wavelength with an accuracy of ±1.4 nm. The detected number of photons was derived from the integrated CCD counts by taking into account the gain, and the wavelength-dependent quantum efficiency of the detector according to the constructor.

Fig. S-1 shows a typical spectral image obtained with a single FEL pulse of 73 eV photon energy and 84 μJ pulse energy. The two Xe superfluorescence lines at 65.18 and 68.14-nm are observed. The spectrum obtained by vertical integration of the image corresponds to the blue line in Fig. 2 of the main text. The vertical axis is the spatial dimension while the horizontal axis is the energy-dispersed dimension. An averaged spectrum that includes the shot-to-shot central wavelength fluctuations has a full-width at half maximum (FWHM) of 0.8 eV.

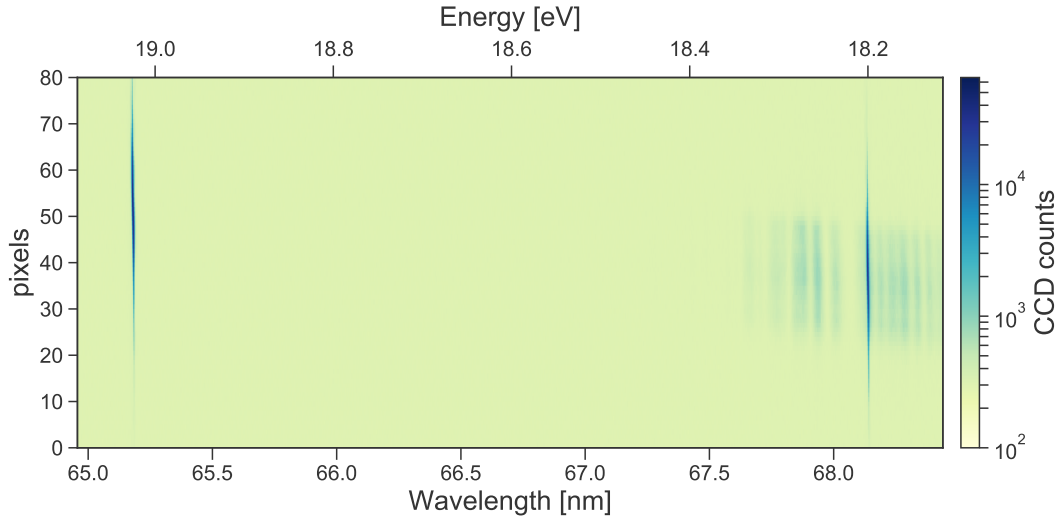

FIG. S-1. Spectral image recorded during a single FEL pulse exposure with 73 eV photon energy and 84 μJ pulse energy. Xe pressure was 7 mbar.

AUGER SPECTRA AND LINE IDENTIFICATION

Xenon

The superfluorescent emission lines observed in Xe are assigned to transitions between Xe^{2+} states which are efficiently populated by Auger decays. The gas - photon interaction at the used XFEL photon energies (73 and 92 eV) leads to the formation of Xe^{+}, Xe^{2+} and Xe^{3+}. Both Xe^{2+} and Xe^{3+} levels can be populated by Auger decay, however analysis of coincidence spectra by Penent et al. [38] revealed that cascade emission of two Auger electrons following ionization in the $4d$ shell is the dominant process of the formation of Xe^{3+} ions. These double decays only lead to the formation of ground state or low energy excitations of Xe^{3+}, with $5s_2 5p_3$ configurations. Radiative transitions between these low-energy excitations and the Xe^{3+} ground state are too low in energy and superfluorescence in Xe^{3+} ions can safely be excluded. The observed lasing transitions are therefore among Xe^{2+} emission lines. The upper and lower states of the transitions could be identified from the literature and especially from the work by Juahiainen et al. [32]. Their assignment is presented in Table S-I.

TABLE S-I. List of the observed XUV stimulated transitions in Xe^{2+}, assigned from Ref. [32] and [35].

λ_L [nm]	Upper state				Lower state			
	Name	Optical designation	Config.	Energy [eV]	Name	Optical designation	Config.	Energy [eV]
65.0479	B	$5s^1 5p^5\ ^1P_1$	0.63 ($5s^2 5p^3 5d$) + 0.23 ($5s^1 5p^5$) + 0.12 ($5s^2 5p^3 6d$)	20.2748	$^3P_1$		$5s^2 5p^4\ ^3P_1$	1.2144
68.2926	B	$5s^1 5p^5\ ^1P_1$	0.63 ($5s^2 5p^3 5d$) + 0.23 ($5s^1 5p^5$) + 0.12 ($5s^2 5p^3 6d$)	20.2748	$^1D_2$		$5s^2 5p^4\ ^1D_2$	2.1200
69.0400		$5s^2 5p^3 5d^1$ ($J = 1$)	$5s^2 5p^3 (^2D^\circ) 5d\ ^3P_1^\circ$	19.1728	$^3P_1$		$5s^2 5p^4\ ^3P_1$	1.2144
108.8954	C	$5s^0 5p^6\ ^1S_0$	$5s^0 5p^6$ ($^1S_0$)	26.1430	A	$5s^2 5p^3 (^2D) 5d\ ^1P_1$	0.65 ($5s^2 5p^3 5d$) + 0.25 ($5s^1 5p^5$)	14.7573

In order to get more details on the population of these Xe^{2+} states, electron-electron coincidence measurements were performed with the HERMES magnetic bottle spectrometer [38, 42] at the SEXTANTS beamline of the synchrotron SOLEIL. Coincidence spectra were recorded for 73 eV and 92 eV photon energies for Xe, and 100 eV photon energy for Kr. Results for Xe are presented in Fig. S-2 and S-3.

First, the branching ratios for the population of Xe^+, Xe^{2+} and Xe^{3+} species was estimated, by comparing the energy spectra of electrons detected in coincidence with 0, 1 or 2 other electrons. These figures take into account the estimated detection efficiency f of the electrons which slowly decreases as a function of the kinetic energy of the photoelectron E_c, from $f = 71\%$ for $E_c = 4$ eV to $f = 58\%$ for $E_c = 80$ eV. The obtained Xe ion ratios are presented in Table S-II. They compare favorably with values from the literature which have been obtained by direct measurement of the ions yields as a function of the photon energy [29].

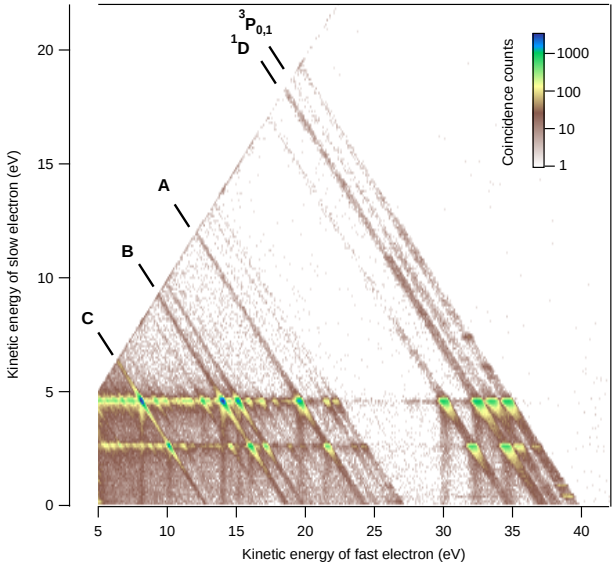

FIG. S-2. Energy correlation map between two electrons detected in coincidence upon photoionization of Xenon atoms with 73 eV photons. The map represents the kinetic energy of the slower electron of the pair (y axis) versus the faster one (x axis). Intensity is encoded in log scale. The two horizontal lines at 2.6 and 4.6 eV are due to the $4d$ photoelectrons. Diagonal lines diagonal lines correspond to formation of the different Xe^{2+} final states. The Xe^{2+} levels involved in the lasing lines are indicated with the same convention as in Table S-I. See text for further details.

Second, the population of the Xe^{2+} final states were investigated in more details, by looking at the energy correlation between the 2 emitted electrons. The energy correlation map between the two electrons emitted upon Xe^{2+} formation by 73 eV photons is presented in Fig. S-2. The diagonal lines correspond to formation of the different Xe^{2+} final states. The Xe^{2+} levels involved in the lasing lines are indicated with the same convention as in Table S-I. The two horizontal lines originate from the $4d$ photoelectrons which are observed here in coincidence with the corresponding Auger electrons. Intensity all along the diagonal lines outside of these $4d$ contributions come from double photoionization in the valence shell. This double photoionization can be a direct or a cascade one, as evidenced respectively by the weak intensity all along the diagonal lines and by the spots on these lines, and as was first shown by Eland et al. (Eland et al, Phys. Rev. Lett. **90**, (2003) 053003). Weak vertical structure originates from false coincidences between Auger electrons and slow energy electrons. From Fig. S-2, we extract the relative contributions of the different processes to the population of the Xe^{2+} final states and especially to the upper and lower states of the observed superfluorescent transitions; they are shown in Fig. S-3 and Table S-III.

73 eV photon energy lies below the $4d$ satellite threshold and it is only the decay of the $4d_{5/2}$ and $4d_{3/2}$ holes which contributes to the Auger decay at this photon energy. At 92 eV the $4d$ satellites to $4d$ main lines ratio is estimated to $11 \pm 1\%$. These satellites decay mainly (73%) by a double Auger path and contribute only marginally to Xe^{2+} population [34]. Population inversion between the superfluorescent states is thus only weakly affected by the contribution of the $4d$ satellite states, which are found to populate relatively more Xe^{2+} excited states than the $4d$ main lines. The main difference between the two photon energies originates from the contribution of the valence double ionization process, which is observed to populate mainly low energy Xe^{2+} final states. Valence double photoionization contributes less at 92 eV photon energy which is close to the maximum of the Xe $4d$ giant resonance [29]. As a conclusion, our coincidence studies show that population inversion is due to the Auger decay of the $4d$ inner-shell holes, and that it is reduced at 73 eV photon energy because of the higher contribution of the valence double ionization path at this photon energy.

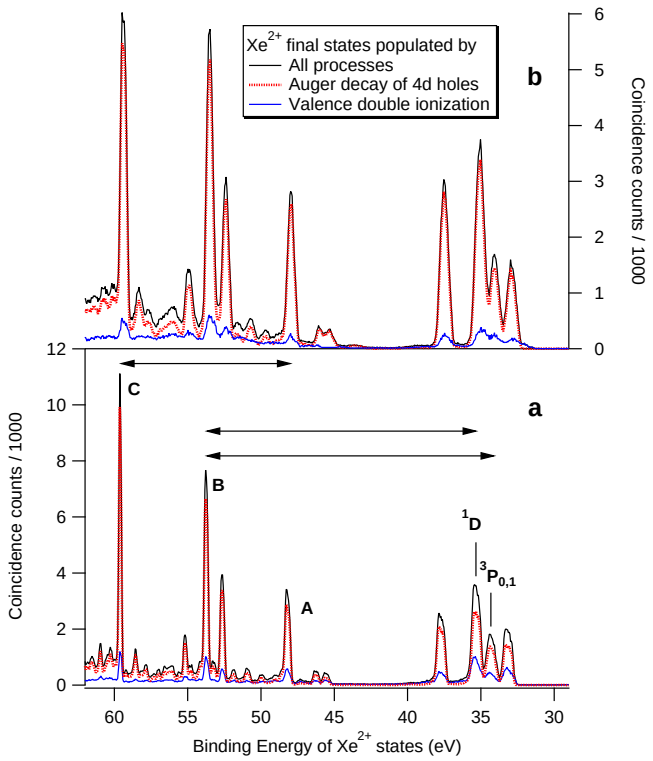

FIG. S-3. Population of Xe^{2+} states by (a) 73 eV and (b) 92 eV incoming photon energies. The horizontal axis shows the sum energy of the two electrons involved in the formation of the Xe^{2+} states. The upper and lower lasing states are shown as well as the different contributing processes ($4d$ hole + Auger decay or valence double ionization). Note that the broader lines observed at the higher photon energy reflect the decreased resolution when the electron kinetic energy increases.

TABLE S-II. Branching ratios in % for the formation of Xe^{n+} ions at the two photon energies examined in our coincidence experiments. They are obtained from the spectra of electrons detected in coincidence with 0, 1 or 2 other electrons. Estimated error bars are ±1 %. They are compared with values estimated from Ref. [29].

	73 eV	73 eV [a]	92 eV	92 eV [a]
Xe^+	27	22	6	7
Xe^{2+}	59	62	65	67
Xe^{3+}	14	16	29	26

[a] Ref. [29]

TABLE S-III. Relative contribution of $4d$ hole Auger decay (including $4d_{5/2}$, $4d_{3/2}$ and $4d$ satellites contributions) versus other processes (direct or cascade valence double ionization) for the population of the upper and lower states of the observed superfluorescent transitions. The last row shows the branching ratios, i.e. the proportion of the Xe^{2+} upper and lower states relative to all Xe^+, Xe^{2+} and Xe^{3+} created by the photon - gas interaction. Note that the $^3P_1$ and the $^3P_0$ are not resolved in our experiment (see Fig. S-2), and that the sum of the two is shown below ($^3P_{0,1}$).

	C		B		A		$^1D_2$		$^3P_{0,1}$	
	73 eV	92 eV	73 eV	92 eV	73 eV	92 eV	73 eV	92 eV	73 eV	92 eV
$4d$ holes	87%	89%	85%	85%	82%	89%	71%	89%	74%	84%
Valence double ionization	13%	11%	15%	15%	18%	11%	29%	11%	26%	16%
Branching ratios	5.8%	7.9%	6.2%	7.8%	3.5%	4.0%	5.7%	6.7%	3.0%	2.7%

Krypton

In Kr, the same reasoning applies. The 100-eV photon energy XFEL beam photoionizes the $3d$ shell with a cross-section of 1.5 Mb. As in the case of Xe at 73 eV, 100 eV is below the shake-up limit. The core-excited states $3d_{3/2}^{-1}$ and $3d_{5/2}^{-1}$, with spin-orbit splitting of 1.26 eV, decay predominantly via Auger processes, forming double ($\approx 70\%$) or triple ($\approx 30\%$) hole states in the $n = 4$ shell.

The simpler atomic structure of Kr with respect to that of Xe allows for ab-initio predictions of the states that correspond to the observed superfluorescent emission. A recent study by Zeng et al. (J. Phys. B: At., Mol. Opt. Phys. **46**, 215002 (2013)) using Flexible Atomic Code (FAC) shows that population inversion occurs in Kr^{2+} but not in Kr^{3+}. Hence, the final excited states of Kr^{2+} are potential candidates for the upper state of the transition observed. The paper of Zeng et al. gives the relative populations of different states of Kr^{2+} and Kr^{3+} after single Auger decay, cascade or double direct Auger decays, but does not give information on further photoemission decay. Therefore, we calculated transition rates and dipole moments in Kr^{2+} using FAC. Population inversion is not sufficient to induce superfluorescence: the transition also requires a strong dipole moment and high transition rate. To take into account the strong electron correlation and configuration mixing, and remain consistent with the Zeng et al. approach, we considered a total of 34 configurations of Kr^{2+}: $4s^24p^4$, $4s^14p^5$, $4s^04p^6$, $4s^24p^25s^2$, $4s^24p^3nl$, $4s^24p^24d^1nl$, $4s^14p^4nl$, $4s^14p^34d^1nl$, $4s^14p^24d^2nl$ and $4s^04p^5nl$ ($nl = 4d, 4f, 5s, 5p$ and $5d$). We could match two lines with significant dipole moments, for which the upper and lower state energies given by Zeng et al. show a sizable population inversion. Their characteristics are presented in Table S-IV. Although FAC accuracy for transition energy is limited to 1 to 2 eV, the calculated line energies are close to the transition observed. The transition from $4s^24p^34d^1$ to $4s^24p^4$ is the one observed by Minnhagen et al., Ark. Fys. (Stockholm) **39**, 471 (1969), (last row of Table S-IV). We could not find any experimental match for the transition from $4s^14p^5$ to $4s^24p^4$ in the literature.

TABLE S-IV. List of the best candidates for the observed XUV stimulated transition in Kr. The wavelength λ_L, energy E_L, transition rate Γ and dipole moment μ as well as the configurations, J number and energies of the levels were calculated using FAC. The Auger decay branching ratios BR as well as the difference δ between Auger decay to upper and lower states according to Zeng et al. are also indicated. The last row shows experimental fluorescence results by Minnhagen et al. of the most probable transition we observed.

λ_L [nm]	E_L [eV]	Γ [10^{10} s^{-1}]	μ [a.u.]	Upper state				Lower state				δ [10^{13} s^{-1}][a]
				Config.	J	E [eV]	BR[a]	Config.	J	E [eV]	BR[a]	
56.331	22.01	2.39	1.45	$4s^24p_{3/2}^34d_{5/2}$	1	26.27	6.1%	$4s^24p_{3/2}^4$	0	4.26	2.8%	1.28
54.135	22.90	2.31	1.35	$4s_{1/2}4p_{1/2}^24p_{3/2}^3$	1	24.97	11.3%	$4s^24p_{1/2}4p_{3/2}^3$	2	2.07	7.0%	1.66
From Minnhagen et al.:												
54.6687	22.6792			$4s^24p^3(^2P^o)4d\ ^3D^o$	1	23.337946		$4s^24p^4\ ^3P$	0	0.65872		

[a] Zeng et al.

ADDITIONAL EXPERIMENTAL DATA

We present here pump energy and gas pressure scans of several emitted lines. The small-signal gain coefficient of the amplification process can be experimentally determined by the pressure dependence of the emission lines at fixed target length (bottom line of Fig. S-4 and Fig. 3-b in the main text). Fitting the exponential rise of the integrated line intensity (dashed lines in Fig. S-4), we determined gain coefficients of the excited medium and summarized them

TABLE S-V. Gain coefficients α extracted from the pressure scans of various superfluorescent lines, as a function of FEL photon energy E_{ph} and pulse energy E_{FEL}.

Line	E_{ph} (eV)	E_{FEL} (μJ)	α (cm^{-1} mbar^{-1})
Xe 65.18 nm	73	30	2.0
Xe 65.18 nm	92	75	5.5
Xe 65.18 nm	100	50	5.3
Xe 109 nm	73	58	0.8
Xe 109 nm	73	58	0.08
Kr 54 nm	100	75	1.0

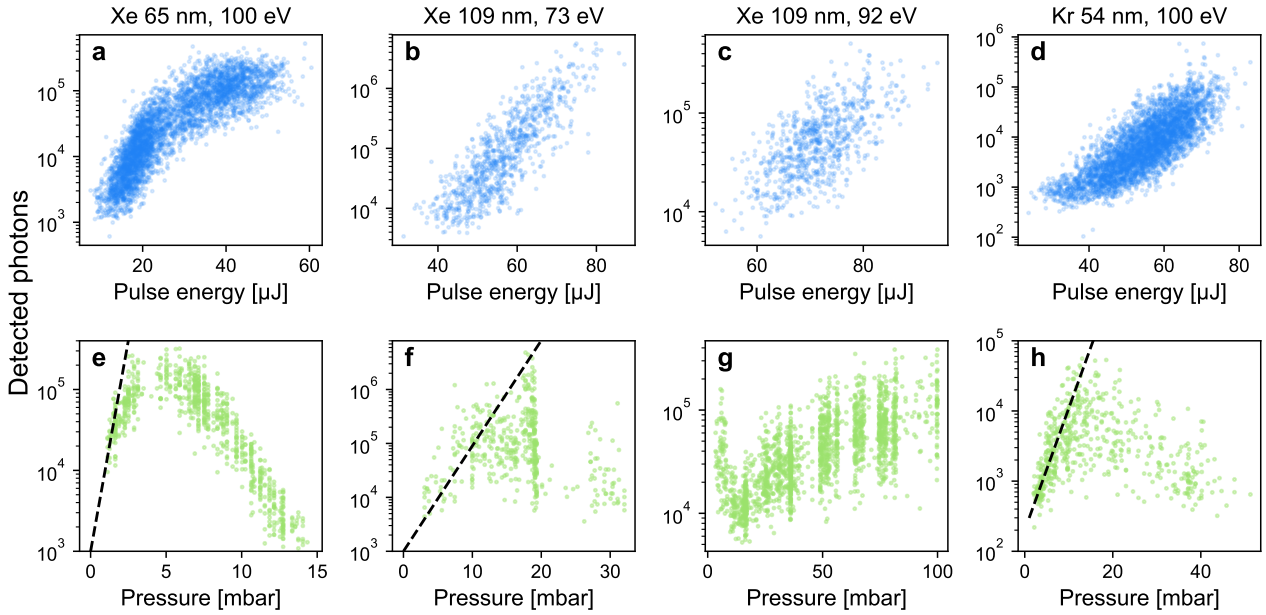

FIG. S-4. Top row: Pump energy scans of observed superfluorescent lines. Average pressure is (a): 5.5 mbar, (b): 10 mbar, (c): 91 mbar, (d): 9.8 mbar. Bottom row: Pressure scans of the same lines. Average pump energy is (e): 50 μJ, (f): 58 μJ, (g): 80 μJ, (h): 75 μJ. The Kr line is observed in 2nd diffraction order, hence the lower detected number of photons with respect to the energy scan (d).

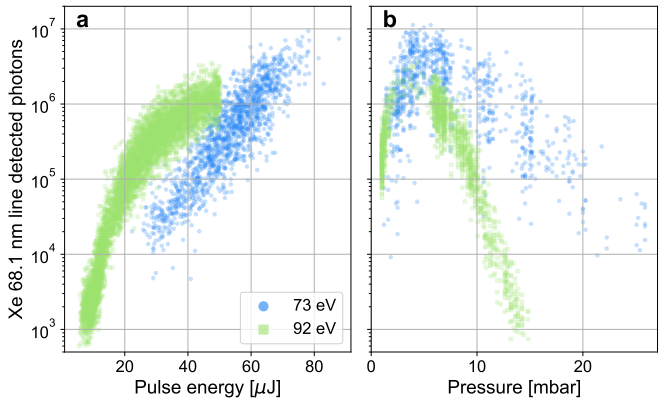

FIG. S-5. Emission yield of the 68.14-nm line as a function of (a) FEL-pulse energy E_P for $\omega_P = 73$ eV (at 7 mbar Xe) and 92 eV (at 3.5 mbar Xe) and (b) pressure for fixed $E_P = 58$ μJ for $\omega_P = 73$ eV and $E_P = 65$ μJ for $\omega_P = 92$ eV.

in Table S-V. We note that the gain coefficient for the Xe 109-nm line pumped with 73 eV is $g' = 0.8$ cm^{-1} mbar^{-1}, which is similar to previous results (Sher et al. [26] observed $g' = 0.73$ cm^{-1} mbar^{-1} for the same Xe 109 nm line). The behaviour of the Xe 109 nm line with 92 eV pump energy is different than the other lines, and no gain coefficient could be extracted. Correlation between the 65-nm line yield and 68-nm line yield is shown on Fig. S-6.

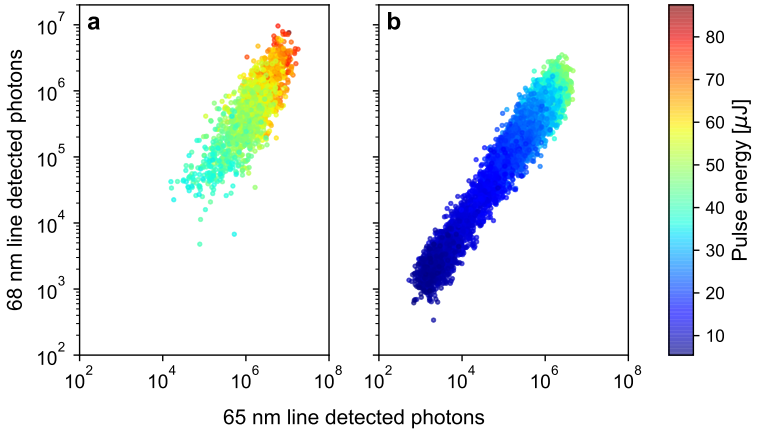

FIG. S-6. Correlation between the 65-nm line yield and 68-nm line yield for (a) 73 eV and (b) 92 eV pump photon energies, Xe gas pressure 7 mbar for 73 eV and 3.5 mbar for 92 eV. The color scale shows the FEL pump energy (in μJ).

DESCRIPTION OF THE SUPERFLUORESCENCE MODEL

Theoretical framework

Here, we describe the few level model for Xe and provide the explicit forms for the time evolution of the populations, correlation function for atomic coherences and the two-point time correlation function for the field operators that gives the temporal and spectral properties of the emitted field. The procedure to obtain these equations is summarized, while a detailed derivation is presented in [15].

Starting from the Hamiltonian (within the rotating wave approximation) for the quantized fields interacting with a set of uniformly distributed two-level atoms, the Heisenberg equations of motion for the field and atomic operators were derived. The field elimination was then performed to express the evolution of atomic operators for a given atom in terms of atomic operators of given and other atoms at previous time moments and field operators at initial time moment. Following this, Weisskopf-Wigner approximation was performed on the terms corresponding to the radiation reaction (spontaneous emission). In order to obtain numerical solutions with moderate computational effort and to allow for parameter studies, a one-dimensional approximation is performed. In addition, using the swept-pumping property leads to time evolution equations in the moving frame of the field. Finally, the time evolution equations for the field and atomic operators were used to evaluate various time and space correlation functions required to obtain the experimentally relevant observables. The higher order correlation functions appearing in the time evolution, beyond second order, were suitably factorized to obtain closed form equations.

In a real system, multiple atomic levels beyond the two lasing levels are involved. The feeding and the depletion of the lasing levels from/to other atomic levels due to pumping and non-radiative decay mechanisms was treated using suitable Lindbladian terms of a corresponding master equation. The influence of these terms on the evolution of the correlation functions was computed following Scully et al., *Quantum Optics*, Cambridge (1997), Ch.8.

The sample in the experiment is assumed to be a quasi one-dimensional medium with a characteristic radius R. For a given three-dimensional density n_3, the one-dimensional density is given as $n_1 = n_3\pi R^2$. The one-dimensional approximation introduces a solid angle parameter, denoted as Δo, the angle into which the atoms are emitting coherently. This approximation can be justified for systems that have Fresnel number about 1, see [2] for further discussions. To take this into account we divide the medium into subregions (along the transverse direction) with Fresnel number 1, take Δo according to dimensions of the subregion and assume radiation from subregions to be independent.

The emission at a given superfluorescence frequency, $\omega_{\rm F}$, is modeled to be a consequence of the following process: The ground state $|0\rangle$ of Xe is pumped by a FEL pulse at central frequency, $\omega_{\rm pump}$. This creates $4d^{-1}$ inner valence-hole state $|c\rangle$ which decays by an Auger process into states that predominantly have $5s^{-1}$ and $5p^{-1}$ hole nature. These states constitute the superfluorescence levels $|g\rangle, |e\rangle$. The fluorescence rate between these levels is denoted by Γ_{sp}. The Auger (super Coster-Kronig) decay of the levels $|g\rangle$ and $|e\rangle$ is energetically closed. The Auger lifetime ($1/\gamma_a$) of

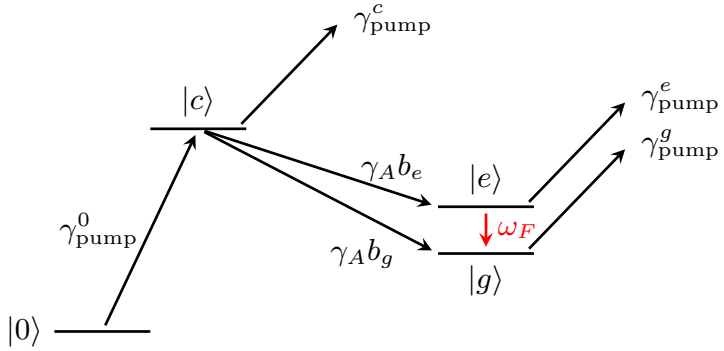

FIG. S-7. Few level model used to simulate Xe superfluorescence. Description is in the text below.

$|c\rangle$ is 6 fs. The branching ratios (b_g, b_e) into the individual lasing levels are estimated from coincidence measurements. The pumping frequency of 73 eV is in the vicinity of the so-called giant resonance feature. The photoionization cross sections of all the states involved are comparable and denoted as σ_{abs}.

The only mechanism responsible for decoherence which we employ in our model is spontaneous emission. It determines the decay term for the polarizations and correspondingly the decay term for the two-point space correlation function of atomic coherences $S(z_1, z_2, \tau)$. The decoherence due to electron collisions could be easily incorporated in the formalism presented below (see A. Benediktovitch, V. Majety, N. Rohringer, Phys. Rev. A **99**, 013839 (2019) for details regarding the general case). However, the value of collisional quenching coefficient in Xe gas is about 0.02 (mbar nsec)$^{-1}$ (according to H. C. Kapteyn and R. W. Falcone, Phys. Rev. A **37**, 2033 (1988)). According to this value, one obtains that even for the highest analyzed pressure of 20 mbar the corresponding lifetime is about 2.7 nsec. It is several times longer than the spontaneous lifetime (1 nsec) and much longer than the simulated timescales for the evolution in the system close to saturation. For this reason the collisional broadening was neglected. The potential influence on Doppler broadening is discussed below.

The pumping rate for a given state $|a\rangle$ is given by $\gamma^a_{pump} = \sigma_{abs} J$, where $J := J_0(z,\tau)\mathcal{G}(z)$ is the pump flux, a function of 1-D space (z) and the retarded time (τ) variables; $J_0(z,\tau) = P_0(z,\tau)/w_0^2$ is the pump flux at beam waist located at the center of the medium ($P_0(z,\tau)$ is the pump power and w_0 is the effective beam waist), and $\mathcal{G}(z) = \left(1 + \left(\frac{z}{z_R}\right)^2\right)^{-1}$ is a correction factor to account for the Gaussian beam shape with z_R being the Rayleigh range.

The evolution of pump flux and the populations of the ground state (ρ_0) and $4d^{-1}$ hole state (ρ_c) are given as:

$$\begin{aligned}
\frac{\partial \rho_0(z,\tau)}{\partial \tau} &= -\sigma_{abs}\rho_0(z,\tau)J(z,\tau), \\
\frac{\partial \rho_c(z,\tau)}{\partial \tau} &= -\gamma_A \rho_c(z,\tau) + \sigma_{abs}\left(\rho_0(z,\tau) - \rho_c(z,\tau)\right)\ J(z,\tau), \\
\frac{\partial J_0(z,\tau)}{\partial z} &= -\sigma_{abs} n_3 J_0(z,\tau).
\end{aligned} \tag{S-1}$$

From energetic considerations, the emitted field can also be absorbed by the ground state with a cross-section σ_{absF}. In our current problem, we are in a regime where $\frac{1}{\Gamma_{sp}} \gg \frac{1}{\Gamma_{col}} \gg \tau_{pump}$ and the number of emitted photons is orders of magnitude lesser than the pump photons. Hence, we neglect the influence of the emitted field on the ground state and define an absorption kernel for the field solely based on the ground state populations at the end of pump pulse as

$$\mathcal{A}(z,z') = e^{-\int_{z'}^{z} dz'' \frac{\kappa(z'')}{2}}, \tag{S-2}$$

with

$$\kappa(z) = \sigma_{absF}\ \rho_0(z, \tau_{pump}). \tag{S-3}$$

The time evolution for the populations of upper (ρ_{ee}), lower lasing levels (ρ_{gg}) and the two-point space correlation

function of atomic coherences ($S(z_1, z_2, \tau)$) is given as:

$$
\begin{aligned}
\frac{\partial \rho_{ee}(z,\tau)}{\partial \tau} &= -\Gamma_{sp}\rho_{ee} - J\sigma_{abs}\rho_{ee} + \gamma_A b_e \rho_c - \frac{3\Delta o}{8\pi}\Gamma_{sp} n_1 \int_0^z dz' \mathcal{A}(z,z') S(z,z',\tau), \\
\frac{\partial \rho_{gg}(z,\tau)}{\partial t} &= \Gamma_{sp}\rho_{ee} - J\sigma_{abs}\rho_{gg} + \gamma_A b_g \rho_c + \frac{3\Delta o}{8\pi}\Gamma_{sp} n_1 \int_0^z dz' \mathcal{A}(z,z') S(z,z',\tau), \\
\sigma(z,\tau) &= \frac{1}{2}\left(\rho_{ee} - \rho_{gg}\right), \\
\frac{\partial S(z_1,z_2,\tau)}{\partial \tau} &= -\Gamma_{sp} S(z_1,z_2,\tau) \\
&\quad + \underbrace{\frac{3\Delta o}{8\pi}\Gamma_{sp} n_1 \left(\sigma(z_1,\tau) \int_0^{z_1} dz' \mathcal{A}(z_1,z') S(z',z_2,\tau) + \sigma(z_2,\tau) \int_0^{z_2} dz' \mathcal{A}(z_2,z') S(z_1,z',\tau) \right)}_{\text{Stimulated emission}} \\
&\quad + \underbrace{\frac{3\Delta o}{8\pi}\Gamma_{sp} \left(\sigma(z_1,\tau)\rho_{ee}(z_2,\tau)\Theta(z_1-z_2)\mathcal{A}(z_1,z_2) + \sigma(z_2,\tau)\rho_{ee}(z_1,\tau)\Theta(z_2-z_1)\mathcal{A}(z_2,z_1) \right)}_{\text{Spontaneous emission}}.
\end{aligned}
\tag{S-4}
$$

These objects can be used to compute the temporal properties of the emitted field and hence the gain dynamics. The spontaneous intensity and the stimulated intensity are computed as:

$$
\mathcal{I}(z,\tau) = \mathcal{I}_{sp}(z,\tau) + \mathcal{I}_{stld}(z,\tau) \tag{S-5}
$$

where

$$
\begin{aligned}
\mathcal{I}_{sp}(z,\tau) &= \frac{3\Delta o}{32\pi\lambda^2}\Gamma_{sp} n_1 \int_0^z dz' \mathcal{A}(z,z') \rho_{ee}(z',\tau), \\
\mathcal{I}_{stld}(z,\tau) &= \frac{3\Delta o}{32\pi\lambda^2}\Gamma_{sp} n_1^2 \int_0^z dz_1' \mathcal{A}(z,z_1') \int_0^z dz_2' \mathcal{A}(z,z_2') S(z_1',z_2',\tau),
\end{aligned}
\tag{S-6}
$$

which lead us to the number of emitted photons:

$$
\mathcal{N}_{ph}(z) = \Delta o\, \pi R^2 \int_0^\infty d\tau' \mathcal{I}(z,\tau'). \tag{S-7}
$$

Finally, to study the spectral properties of the emitted field, we study the time evolution of two-point time correlation function for field operators, $G(z, \tau_1, \tau_2)$, given as

$$
\begin{aligned}
\frac{\partial G(z,\tau_1,\tau_2)}{\partial z} &= -\kappa(z) G(z,\tau_1,\tau_2) \\
&\quad + \underbrace{\frac{3\Delta o}{8\pi}\Gamma_{sp} n_1 \left(\int_0^{\tau_1} d\tau_1' e^{-\int_{\tau_1'}^{\tau_1} d\tau'' \frac{\Gamma(z,\tau'')}{2}} \sigma(z,\tau_1') G(z,\tau_1',\tau_2) + \int_0^{\tau_2} d\tau_2' e^{-\int_{\tau_2'}^{\tau_2} d\tau'' \frac{\Gamma(z,\tau'')}{2}} \sigma(z,\tau_2') G(z,\tau_1,\tau_2') \right)}_{\text{Stimulated emission}} \\
&\quad + \underbrace{\frac{3\Delta o}{32\pi\lambda^2}\Gamma_{sp} n_1 \int_0^{\min(\tau_1,\tau_2)} d\tau' e^{-\int_{\tau'}^{\tau_1} d\tau'' \frac{\Gamma(z,\tau'')}{2}} e^{-\int_{\tau'}^{\tau_2} d\tau'' \frac{\Gamma(z,\tau'')}{2}} \left(\gamma_{aug} b_e \rho_c(z,\tau') + J(z,\tau')\sigma_{abs}\rho_{ee}(z,\tau')\right)}_{\text{Spontaneous emission}},
\end{aligned}
\tag{S-8}
$$

where

$$\Gamma(z,\tau) = \Gamma_{sp} + 2\sigma_{abs} J(z,\tau) \tag{S-9}$$

is the total decay rate. The spectral properties can then be computed as

$$\mathcal{I}(z,\omega) = \int d\tau_1 \, e^{i\omega\tau_1} \int d\tau_2 \, e^{-i\omega\tau_2} G(z,\tau_1,\tau_2). \tag{S-10}$$

Simulation results

We present here details of the model calculations shown in the main text, for a pump photon energy of 73 eV. A reasonable agreement between the simulations according to equations presented above and the experimental dependence of emitted photon number on FEL pump energy and Xe gas pressure was found for the following simulation parameters: spontaneous lifetime corresponding to the transition from $|e\rangle$ to $|g\rangle$ level is 1 ns; Auger branching ratios are b_e =0.062/3 and b_g =0.030/4, where the measured branching ratios (see Table S-II) are divided by degeneracy of the levels; XFEL absorption cross section σ_{abs}=5.2 Mb, superfluorescence absorption cross section σ_{absF}=60 Mb, pump duration is 80 fs, Gaussian shape is assumed; z_R =2.0 mm, effective photon flux varies from 8.7×10^8 photons/μm^2 at 30 μJ to 2.0×10^9 photons/μm^2 at 70 μJ. The sample length is 6.5 mm.

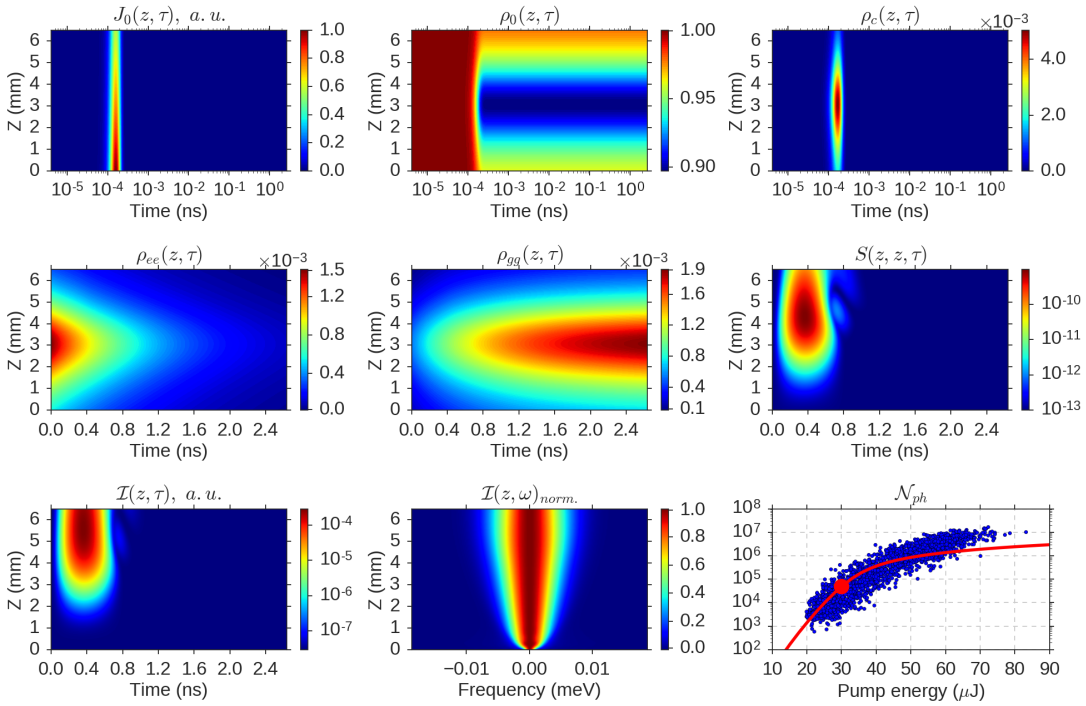

FIG. S-8. Example of the evolution of the system observables in the case of 30 μJ pump pulse energy and 73 eV pump photon energy. The number of emitted photons at this pump energy is shown by a red dot. The emitted radiation spectra for each z value are normalized to maximal value at given z.

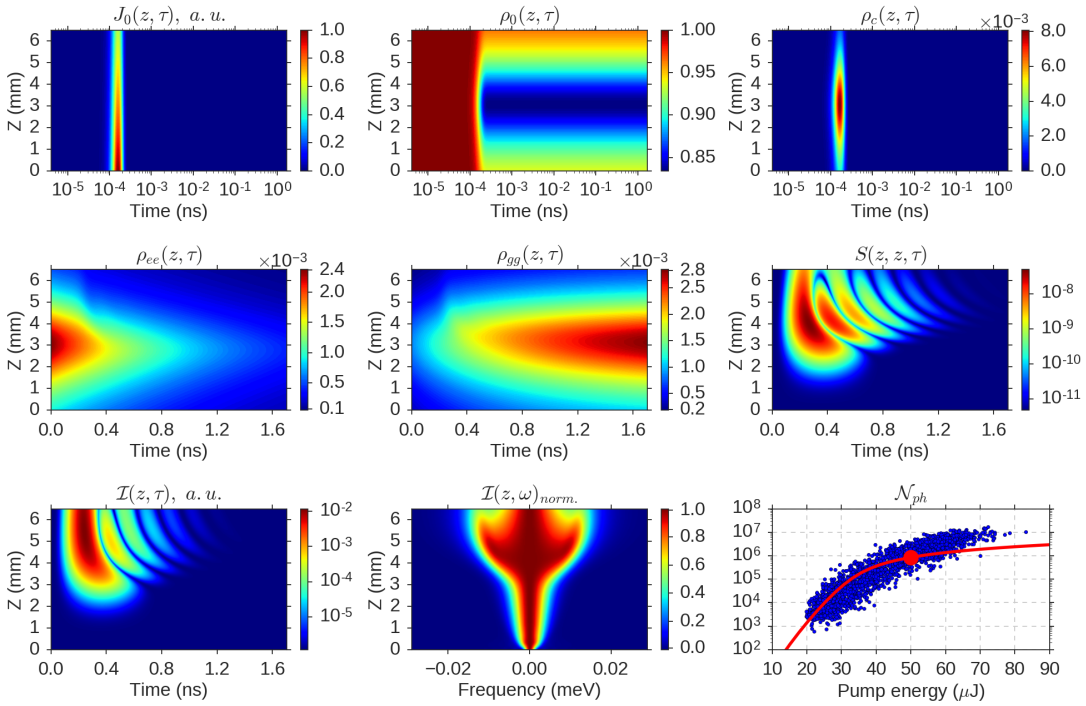

FIG. S-9. Same as Fig. S-8 for 50μJ pumping.

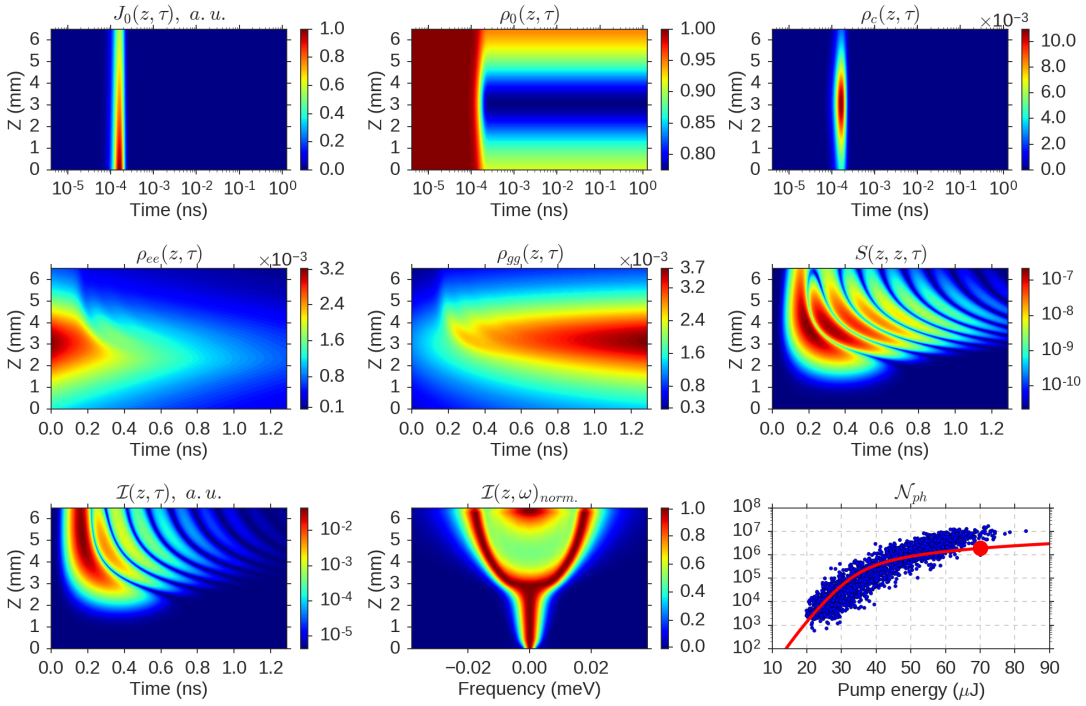

FIG. S-10. Same as Fig. S-8 for 70μJ pumping.

Figures S-8 - S-10 present examples of system observables evolution for various values of pumping. The same parameters as for Fig. 3 of the main text were used. Fig. S-8 demonstrates the case when the superfluorescence is not the dominating channel of atomic deexcitation. A significant part of emitted radiation could still be emitted spontaneously in 4π solid angle that could not be registered at the detector. The typical timescales are about 1 ns that is about radiation lifetime. Also one can see that the correlation between atomic coherences $S(z_1, z_2, t)$ takes the values several orders of magnitude smaller than the values expected at saturation. Hence, at this pump energy, the stimulated emission in forward direction is weak, as result, the emission yield observed on the detector is much smaller than the number of emitters. In particular, the number of emitted photons is about $1. \times 10^6$ (at the exit from the sample, the corresponding value at the detector is about $5. \times 10^4$). The increasing of the pump results in stronger depletion of the ground level and higher population of the core-excited level. It is transferred to higher population of the $|e\rangle$ level at the initial time. This in turn results in higher values of correlation of atomic coherences that leads to collective oscillatory behavior as can be seen in the Figs S-9, S-10. The oscillatory behavior in the temporal domain translates in a broadening of the emitted radiation spectra. The superfluorescent-like behaviour becomes the dominant mechanism of the atom deexcitation. However, the number of emitted photons is smaller than the number of emitters due to absorption. The absorption is strong since the fraction of atoms in the inverted state that amplify the radiation is quite small (about 10^{-3}), the rest of the atoms in the gas are absorbing the emitted radiation. This is one of the reasons of the drop of the yield at higher pressures, see Fig. 3 b of the main text. Under the considered conditions, the calculated absorption length of the emitted superfluorescent radiation is about 1 mm.

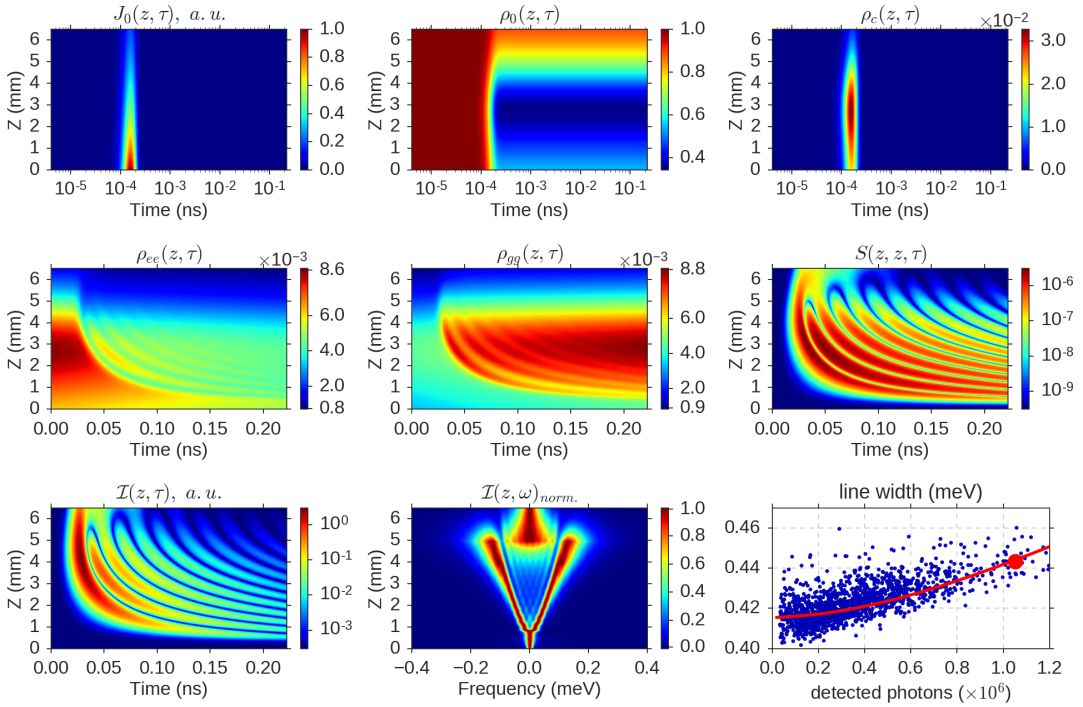

FIG. S-11. Example of the evolution of the observables for 68-nm transition (under conditions corresponding to Fig. 4 of the main text) for 70 μJ pump-pulse energy. The last plot in the series shows the ensemble of experimentally measured line width as a function of detected number of photons. The preceding plots correspond to the experimental condition marked by the red dot. Further, we show the theoretically deduced line width for lower pump-pulse energies, that have been determined by convolution of the theoretical results with a Gaussian instrumental function of 0.415 meV width.

Due to similar Auger-branching ratios, the behaviour of the 65-nm line and the 68-nm line are similar. This is also evident from the strong correlation of the photon yields of the 65- and 68-nm emission lines presented in Fig. S-6. Since both of the emission lines are subject to one shared upper level, a more thorough theoretical analysis would need to resort to a more complex level scheme. In our opinion, our 1D approach is the most severe approximation limiting the quantitative comparison of theory and experiment. We therefore consider two independent emission lines.
Due to limitations in beam time, measurements of the line shapes could only be conducted for the 68-nm emission

line. In particular, the measurements of the 68-nm transition line shape (Fig. 4 of the main text) were done during a different experimental run than those of pressure and pump-energy scans (Fig. 3 of the main text), and therefore in different experimental conditions. In particular, the line-shape measurements were in 3rd order of the diffraction grating for improved resolution. To enhance the signal-to-noise ratio, the CCD integrated the signal from a train of 3 FEL pulses, each separated by 1μs and with different pulse energy. During this measurements, the pressure in the cell was varied between 30 and 44 mbar and showed no correlation with the line width. Due to rarefaction waves induced in the pressurized cell, each pulse of the 3 consecutive pulses finds a medium of different effective pressure (the second and third pulse sees a strongly diluted medium). We therefore adapted our theoretical model and found that an effective pressure of 20 mbar (in contrast to 7 mbar pressure for the pressure- and pump-energy scans) agreed with the experimental findings. The effective pump-photon flux was assumed as 1.3×10^{10} photons/μm^2 for $E_P = 70$ μJ and the other parameters remained unchanged from those of Fig. S-10. Fig. S-11 shows the details of evolution for the case of 70 μJ pump energy: As evident from the evolution of the emitted intensity as a function of time and propagation distance, the optical density for this particular set of parameters results in re-absorption of the emitted radiation. This implies, that the maximum number of photons, maximum peak intensity and concurrent width it the largest line width (broadening) would be observed for shorter propagation distances than the actual length of the medium. Due to a larger number of emitters (higher pressure, tighter focusing), the superfluorescence-like behaviour is more pronounced as compared to the conditions of Fig. S-10. Due to the reabsorption in the medium, the total number of emitted photons is comparable to that of Fig. S-10 and is not a good measure for saturation.

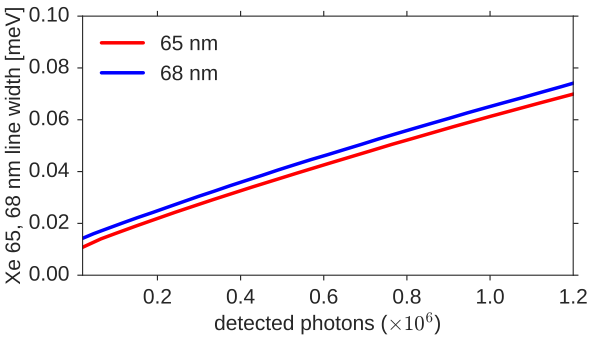

FIG. S-12. Calculated width (FWHM) of the 65- and 68-nm emission line as a function of the number of detected photons, assuming a 5 % detection efficiency.

The calculated dependence of the emission-line width as a function of the number of detected photos is depicted in Fig. S-12. The figures shows a comparison between the 65- and 68-nm emission lines. Within our theoretical model, the widths are comparable.

Influence of Doppler broadening

The Doppler effect for Xe atoms at ambient temperature (corresponding to measurement conditions) results in Gaussian broadening with FWHM about $\Delta E_{Doppler} = 0.02$ meV. It is about 20 times smaller than the instrumental broadening of the spectrometer and several times smaller than the broadening due to superfluorescence-like behaviour at saturation (see Fig. 4 a, c of the main text). The Doppler broadening could play a role at the initial amplification stages [F. A. Hopf and P. Meystre, Phys. Rev. A **12**, 2534 (1975)]. An accurate treatment of Doppler broadening would require the consideration of the distribution of polarizations and their evolution, instead of considering of a single value. Adding this level of complexity is beyond the scope of the present approach. A way to estimate the influence of dephasing due to Doppler broadening is to phenomenologically introduce a dephasing time T_2 that would correspond to the inverse Doppler width. Although this approach is not rigorous it has been shown that it can reliably mimic the impact of Doppler broadening in the initial stages of amplified spontaneous emission in gain-swept geometry [M.F.H. Schuurmans, Opt. Commun. **34**, 185 (1980)] and gives results in quantitative agreement with a more rigorous treatment. We therefore adopted this simplified approach to assess the importance of Doppler broadening in our case. Fig. S-13 shows a comparison of the pump-energy dependence of the emission yield of the 65-nm line with and without Doppler broadening. The pump-energy dependence is shown for several effective focal waists. As evident from the plot, the introduction of Doppler dephasing is qualitatively equivalent to the case of no

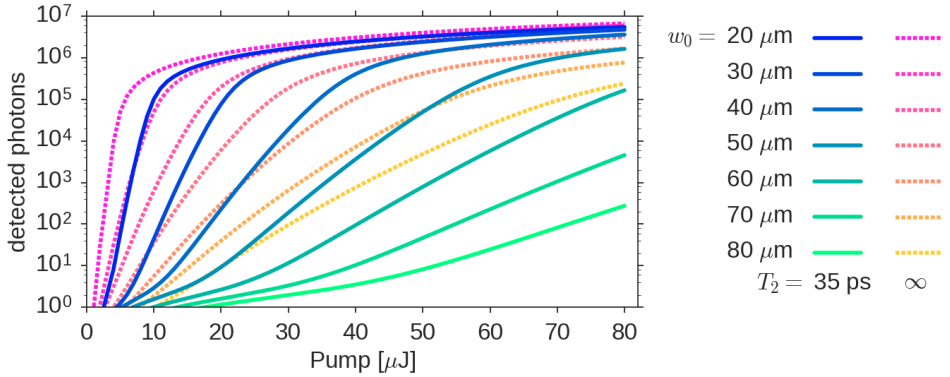

FIG. S-13. Emission yield of the 65-nm line as a function of FEL-pulse energy E_P (for parameters corresponding to Fig. 3 a of the main text) modeled without taking the Doppler broadening into account (dotted lines) and accounting for Doppler broadening in terms of a decoherence time $T_2 = \hbar/\Delta E_{Doppler} = 35$ ps (solid lines). The series of lines corresponds to variation of the effective beam waist w_0 which is a parameter of the 1D model.

Doppler dephasing for a system of larger beam waist. We expect that the restriction of our model to 1D introduces more uncertainty in the quantitative description than the inclusion of Doppler broadening.